

# 000 001 002 003 004 005 LEARNING LOCAL EQUIVARIANT REPRESENTATIONS 006 FOR QUANTUM OPERATORS 007 008 009

010 **Anonymous authors**  
 011 Paper under double-blind review  
 012  
 013  
 014  
 015  
 016  
 017  
 018  
 019  
 020  
 021  
 022  
 023  
 024  
 025  
 026  
 027

## ABSTRACT

028 Predicting quantum operator matrices such as Hamiltonian, overlap, and density  
 029 matrices in the density functional theory (DFT) framework is crucial for material  
 030 science. Current methods often focus on individual operators and struggle with ef-  
 031 ficiency and scalability for large systems. Here we introduce a novel deep learning  
 032 model, SLEM (strictly localized equivariant message-passing) for predicting mul-  
 033 tiple quantum operators, that achieves state-of-the-art accuracy while dramatically  
 034 improving computational efficiency. SLEM’s key innovation is its strict locality-  
 035 based design for equivariant representations of quantum tensors while preserving  
 036 physical symmetries. This enables complex many-body dependency without ex-  
 037 panding the effective receptive field, leading to superior data efficiency and trans-  
 038 ferability. Using an innovative SO(2) convolution and invariant overlap parameter-  
 039 ization, SLEM reduces the computational complexity of high-order tensor prod-  
 040 ucts and is therefore capable of handling systems requiring the  $f$  and  $g$  orbitals in  
 041 their basis sets. We demonstrate SLEM’s capabilities across diverse 2D and 3D  
 042 materials, achieving high accuracy even with limited training data. SLEM’s de-  
 043 sign facilitates efficient parallelization, potentially extending DFT simulations to  
 044 systems with device-level sizes, opening new possibilities for large-scale quantum  
 045 simulations and high-throughput materials discovery.

## 046 1 INTRODUCTION

047 Quantum operators, representing observables and the evolution of quantum systems, are the corner-  
 048 stone of describing the microscopic world. In modern quantum science, the advent of density func-  
 049 tional theory (DFT) Hohenberg & Kohn (1964); Kohn & Sham (1965) has elevated single-particle  
 050 quantum operators, such as the Kohn-Sham Hamiltonian, density matrix, and overlap matrix, to  
 051 paramount importance in solving complex problems Jones (2015). These operators play a crucial  
 052 role in unravelling electronic structures, predicting material properties, and advancing quantum tech-  
 053 nologies. However, as we tackle larger and more complex systems, these fundamental operators’  
 054 efficient and accurate representation has emerged as a pressing challenge in computation, demanding  
 055 new avenues for innovative methodologies.

056 Recent advances have incorporated machine learning (ML) techniques to accelerate DFT calcu-  
 057 lations by directly predicting DFT’s output of quantum operators, including charge density Unke et al.  
 058 (2021), overlapping matrix Yu et al. (2023); Unke et al. (2021), self-energy Dong et al. (2024),  
 059 wave function Unke et al. (2021), and Hamiltonian matrix Yin et al. (2024); Yu et al. (2023); Gong  
 060 et al. (2023); Nigam et al. (2022); Unke et al. (2021); Zhong et al. (2023). By circumventing self-  
 061 consistent DFT calculations, such methods have the potential to scale up the electronic structure  
 062 calculations. Some of the approaches utilize Gaussian regressions Nigam et al. (2022), kernel-based  
 063 models Nigam et al. (2022), and neural networks Li et al. (2022) to predict invariant Hamiltonian  
 064 matrix blocks on localized frames. Notably, powerful equivariant message-passing neural networks  
 065 (E-MPNNs) have demonstrated remarkable accuracy Han et al. (2024); Musaelian et al. (2023);  
 066 Batatia et al. (2022); Joshi et al. (2023); Liao & Smidt (2022); Liao et al. (2023); Simeon & De Fab-  
 067 ritiis (2024); Passaro & Zitnick (2023); Zitnick et al. (2022). These networks ensure the output  
 068 tensor blocks’ equivariance, respecting atomic systems’ physical priors. Typically, they use iterative  
 069 updates to build many-body interactions, achieving high accuracy while enlarging the receptive field.  
 070 This limits parallelization and, consequently, the model’s scalability. The storage-intensive quantum

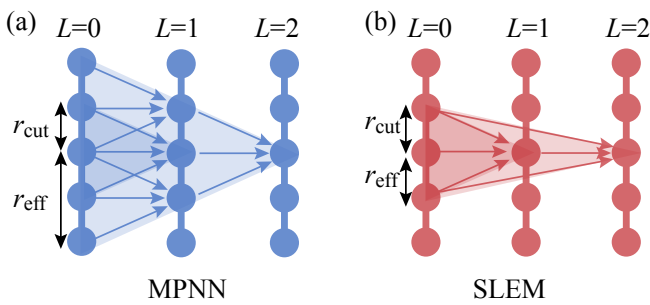


Figure 1: Local design of SLEM vs MPNN on 1D graph.(a) MPNN aggregation. (b) SLEM aggregation. Balls: nodes, sticks: edges, arrows: aggregation direction.  $r_{\text{cut}}$ : predefined cutoff;  $r_{\text{eff}}$ : effective cutoff after 2 layer updates.  $L$ : layer index.

tensor prediction tasks exacerbate these limitations, posing considerable challenges for training such models on large datasets or predicting quantum operators for extensive atomic structures .

Fortunately, the electrostatic screening counteracts the long-term dependency in a lot of material systems Huckel & Debye (1923); Resta (1977); Ninno et al. (2006). Therefore, quantum operators can be decomposed into elements dependent locally on atomic structures, which naturally prefers a strictly local model that avoids expanding the receptive field. The Allegro model Musaelian et al. (2023) applied this concept to build ML interatomic potentials (MLIPs), achieving high accuracy and parallelizability. While MLIPs only concern scalars (energy) and vectors (forces) (angular momentum  $l = 0$  and 1) on each node, predicting quantum operators necessitates targeting both node and edge features on high-order spherical tensors (even up to  $l = 6$  or 8). This requires locality and representability for both node and edge. Another significant challenge is computational complexity. To equivariantly mix the features of different angular momentum  $l$ , tensor products that scale as  $\mathcal{O}(l^6)$  are required Passaro & Zitnick (2023). This makes model training, especially on heavy atoms, extremely slow. This limitation hinders the development of a unified ML DFT model that generalizes across the periodic table.

This work presents a novel method, the strictly localized equivariant message-passing model (SLEM), for efficient representations of quantum operators. SLEM employs a fully localized scheme to construct high-order node and edge equivariant features for a general representation of quantum operators, including the Hamiltonian and density matrix. As illustrated in Fig. 1, the model embeds localized edge hidden states and utilize them to construct localized node and edge features without including distant neighbours beyond a fixed cutoff range  $r_{\text{cut}}$ . This design enables the SLEM model to generalize better, parallelize easier, and scale to larger systems. Additionally, a fast and efficient SO(2) convolution Passaro & Zitnick (2023) is implemented to reduce the  $\mathcal{O}(l^6)$  complexity, with edge-specific training weights, thereby further enhancing the model’s accuracy. As for the overlap matrix, it is typically required for property calculations. Previous works have used another E-MPNN that doubles the network sizes Zhong et al. (2023) or extracts it from DFT calculations Gong et al. (2023); Yu et al. (2023), incurring additional costs or incorporating out-of-loop computation steps that complicate inference. In contrast, we utilized the two-centre integrals and parameterized the overlap matrix with spherical independent scalars (i.e., Slater-Koster (SK) parameters Slater & Koster (1954)). This method, inspired by the work of DeePTB Gu et al. (2023), fits the overlap operator representation with minimal additional cost.

## 2 RELATED WORKS

**Message-passing Neural Networks** Message-passing neural networks (MPNNs) Gilmer et al. (2017) have been widely applied in the modelling of atomic systems due to their exceptional accuracy in capturing the intricate relationships between atomic environments and physical properties Schütt et al. (2020). Previous works have predominantly utilized this scheme, achieving remarkably high precision in reported systems Schütt et al. (2018); Satorras et al. (2021); Han et al. (2024). However, as the MPNNs updates, the effective cutoff radius ( $r_{\text{eff}} = N \times r_{\text{cut}}$ ) for each atom’s features

grows linearly with the number of update steps ( $N$ ), as shown in Fig. 1. Consequently, the effective neighbour list scales cubically with  $r_{\text{eff}}$ , making parallelization intractable. Allegro Musaelian et al. (2023) achieved locality modifies the updating rules by incorporating a hidden atom-pair state that depends partially on the centre atom. While this framework works successfully for scalars and  $l=1$  vectors in potential energy prediction, it requires further improvement for fitting more general edge and node features. Other local methods avoid iterative updates that enlarge the receptive field, instead creating manually designed descriptors of the local environment Behler & Parrinello (2007); Bartók et al. (2010); Thompson et al. (2015); Zhang et al. (2018a); Wang et al. (2018); Zhang et al. (2018b). These methods are generally local, but often balance locality and representation capacity.

**Equivariant Message Passing** Physical quantities, under the law of nature, should be invariant or equivariant under the spatial and temporal symmetry operations. To model such quantities, a set of neural network models has been developed utilizing equivariant operations. Thomas et al. (2018); Weiler et al. (2018); Kondor et al. (2018); Kondor (2018) These neural networks possess physical priors to ensure outputs transform in sync with inputs, making them more generalizable, accurate, and data-efficient in predicting physical quantities. Formally, an equivariant operation from vector space  $X$  to  $Y$  is defined such that:

$$f(D_X[g]\mathbf{x}) = D_Y[g]f(\mathbf{x}) \quad \forall g \in G, \forall \mathbf{x} \in X$$

where  $D_X[g] \in GL(X)$  is the representation of group element  $g$  on vector space  $X$ . Here we consider  $O(3)$  group, then  $\mathbf{x}, \mathbf{y}$  can be composed by irreducible representation (irreps for short) that are the spherical tensors with angular and magnetic momentum index  $l, m$ , and parity  $p$  such that  $|m| \leq l$ . Irreps with the same  $l$  support addition/subtraction, while a generalized multiplication is defined as tensor product ( $\otimes$ ):

$$(\mathbf{x} \otimes \mathbf{y})_{m_3}^{l_3} = \sum_{m_1, m_2} C_{(l_1, m_1)(l_2, m_2)}^{(l_3, m_3)} \mathbf{x}_{m_1}^{l_1} \mathbf{y}_{m_2}^{l_2}$$

Where  $C_{(l_1, m_1)(l_2, m_2)}^{(l_3, m_3)}$  are Clebsch-Gordan (CG) coefficients. Conventional tensor product has the time and memory scales of  $O(l_{\max}^6)$  Passaro & Zitnick (2023) where  $l_{\max}$  is the maximum angular momentum in  $\mathbf{x}$  and  $\mathbf{y}$ . Such complexity poses great challenges for quantum tensor prediction. For example, constructing blocks of  $f\text{-}f$  and  $g\text{-}g$  orbital pairs require irreps of maximum order  $l = 6$  and  $l = 8$ . Such high costs make training for large-size systems nearly impossible.

### 3 MODEL ARCHITECTURE

#### 3.1 PARAMETERIZE EQUIVARIANT QUANTUM OPERATORS

The equivariant parameterization of quantum operators  $\hat{O}$ , such as the Hamiltonian and density matrix in the LCAO-based DFT framework, is illustrated in Fig. 2. The matrix element of operator  $\hat{O}$  can be expressed as:

$$O_{l_1, l_2, m_1, m_2}^{i,j} = \langle i, l_1, m_1 | \hat{O} | j, l_2, m_2 \rangle \quad (1)$$

Here  $i$  and  $j$  denote atomic sites, while the angular and magnetic momentum index  $l, m$  label the atomic orbitals of the site. We apply the Wigner-Eckart theorem to decomposes the operator indexed by  $l_1, l_2$  into a single index  $l_3$  that satisfies  $|l_1 - l_2| \leq l_3 \leq (l_1 + l_2)$ :

$$o_{l_3, m_3}^{i,j} = \sum_{l_1, m_1, l_2, m_2} C_{(l_1, m_1)(l_2, m_2)}^{(l_3, m_3)} O_{l_1, l_2, m_1, m_2}^{i,j} \quad (2)$$

Here, the edge ( $i \neq j$ ) and node ( $i = j$ ) features  $o_{l_3, m_3}^{i,j}$  are grouped by the index  $m$  into vectors of  $\mathbf{o}_{c,l}^{i,j}$  with  $c$  accounting for multiple tensors for the same  $l$ . These features can be computed for hopping ( $i \neq j$ ) and onsite ( $i = j$ ) elements of the quantum operators. Further, by leveraging the Hermitian nature of quantum operators, the parameterized elements can be reduced to upper diagonal blocks. This is almost half the demanding storage. Then, we standardised  $\mathbf{o}_{c,l}^{i,j}$  to balance the variance. Formally:

$$\mathbf{o}_{c,l}^{i,j} = \sigma_{c,l}^{Z_i, Z_j} \hat{\mathbf{o}}_{c,l}^{i,j} + \mu_{c,l}^{Z_i, Z_j} \delta_{l,0} \quad (3)$$

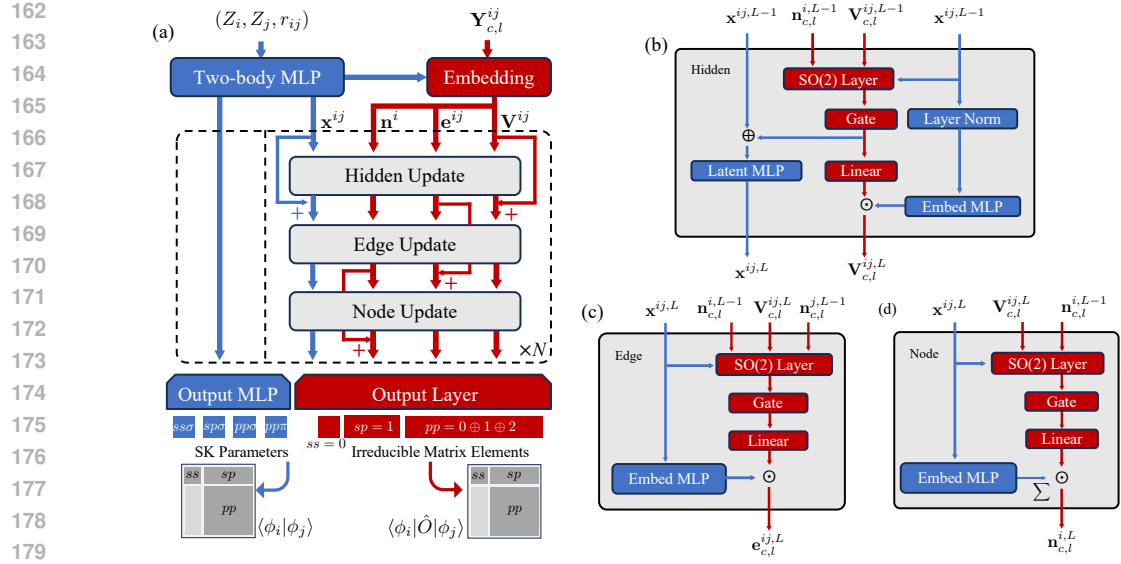


Figure 2: Design of the SLEM model. (a) Hierarchical structure of the model. Starts with the atomic number  $Z_i$ , the radial and spherical part of the shift vector  $r_{ij}$  and  $\mathbf{Y}_{c,l}^{ij}$ , the initialized hidden features  $\mathbf{x}^{ij}$ ,  $\mathbf{V}^{ij}$ , along with edge and node features  $\mathbf{e}^{ij}$ ,  $\mathbf{n}^i$ , are generated. The two-body hidden features predict the SK parameters constructing (off-)diagonal blocks for the overlap operator. Others features are then iteratively updated using the designed strictly localized updating scheme. (b)-(d) shows the hidden update (b), edge update (c), and node update (d). Node and edge features are used to construct the diagonal blocks for quantum operators.

Here,  $Z_i$ ,  $Z_j$  are the atom species of atom  $i$  and  $j$ ,  $\sigma_{c,l}^{Z_i, Z_j}$  and  $\mu_{c,l}^{Z_i, Z_j}$  are norm and bias value for each atom and atom-pair. These values are derived from the dataset statistics and applied as weights and biases in an atom/bond type-specific scaling layer. This step helps to resolve the unbalanced norms across diagonal and off-diagonal elements of quantum operators while facilitating using a ReLU-activated network to learn the normalized radial dependent decaying function from 1 to 0.

After supervising on the normalized features  $\hat{o}_{c,l}^{i,j}$ , inverse transform from Eq. 2 is applied to reconstruct the predicted operator representations such as Hamiltonian and density matrix blocks:

$$O_{l_1, l_2, m_1, m_2}^{i,j} = \sum_{l_3, m_3} C_{(l_1, m_1)(l_2, m_2)}^{(l_3, m_3)} o_{l_3, m_3}^{i,j} \quad (4)$$

The whole procedure satisfies the rotational, transformational and reflectional symmetry.

### 3.2 PARAMETERIZE OF INVARIANT OVERLAP OPERATORS

The overlap matrix, analogous to other quantum operators, is defined as:

$$S_{l_1, l_2, m_1, m_2}^{i,j} = \langle i, l_1, m_1 | j, l_2, m_2 \rangle = \int \phi_{m_1}^{i, l_1}(\mathbf{r}) \phi_{m_2}^{j, l_2}(\mathbf{r} - \mathbf{r}_{ij}) d\mathbf{r} \quad (5)$$

where  $\phi_m^{i,l}$  is the orbital from LCAO bases. The overlap matrix also satisfies the equivariance relation. Since the equivariant dependency comes fully from the bases, it is possible to rotate them to align with the axis of  $\mathbf{r}_{ij}$ , reducing the angular dependence. Therefore, we can further simplify the matrix elements into scalars via the relation Podolskiy & Vogl (2004):

$$\int \phi_{m_1}^{i, l_1}(\mathbf{r}) \phi_{m_2}^{j, l_2}(\mathbf{r} - \mathbf{r}_{ij}) d\mathbf{r} = s_{l_1, l_2, |m_1|}^{Z_i, Z_j}(r_{ij}) \delta_{m_1, m_2} \quad (6)$$

Here, the dependency changes to  $Z_i$ ,  $Z_j$ , and  $r_{ij}$ , indicating the two-center nature of the overlap integrals. Parameterizing these distance-dependent radial functions involves encoding atomic species

216 with radial information and a simple MLP to learn the mapping to target scalars.  
 217

$$f_{l_1, l_2, |m|}(Z_i, Z_j, r_{ij}) = s_{l_1, l_2, |m_1|}^{Z_i, Z_j}(r_{ij}) \delta_{m_1, m_2} \quad (7)$$

220 After getting these parameters, we use them to construct the overlap matrix aligned with the bond  
 221 axis, and then rotate it back to the original orientation.

### 222 3.3 THE SLEM MODEL

224 The SLEM model architecture is illustrated in Fig. 2. The model maintains a set of features, in-  
 225 cluding hidden features  $\mathbf{x}^{ij, L}$ ,  $\mathbf{V}_{c, l}^{ij, L}$ , node features  $\mathbf{n}_{c, l}^{i, L}$  and edge features  $\mathbf{e}_{c, l}^{ij, L}$  of hidden layer ( $L$ ).  
 226 Specifically, the hidden features consist of a scalar channel  $\mathbf{x}^{ij, L}$  and a tensor channel  $\mathbf{V}_{c, l}^{ij, L}$ . The  
 227 scalar channel is initialized as an embedded vector containing two-body information, including the  
 228 atomic species and the radial distance of the atom pair. These initialized two-body radial features  
 229 are then mapped by an MLP to the invariant SK parameters for overlap. For equivariant quantum  
 230 operators, such as the Hamiltonian and density matrix, the scalar and tensor channels interact to  
 231 generate an ordered atom-pair representations, which are used to construct local node and edge rep-  
 232 resentations. After iterative updates, the representation is scaled by the statistical norm and biases,  
 233 thereby achieving the final prediction.

#### 235 3.3.1 FEATURE INITIALIZATION

237 Firstly, the initial scalar hidden feature is computed from the two-body embeddings of atomic species  
 238  $Z_i$  and  $Z_j$ , and the radial distance  $r_{ij}$ , as follows:

$$\mathbf{x}^{ij, L=0} = \text{MLP}_{\text{2-body}}(\mathbf{1}(Z_i) \parallel \mathbf{1}(Z_j) \parallel \mathbf{B}(r_{ij})) \cdot u(r_{ij}) \quad (8)$$

241 Here,  $\parallel$  stands for vector concatenation, atom species are embedded with one-hot vectors denoted as  
 242  $\mathbf{1}(Z)$ , and a set of trainable Bessel bases  $\mathbf{B}(r_{ij})$  is utilized to encode the distance  $r_{ij}$  between atoms  
 243  $i$  and  $j$ .  $u(r_{ij})$  are envelope functions Batzner et al. (2022) to add explicit radial dependence. Sub-  
 244 sequentially, the edge and hidden features are initialized as weighted spherical harmonics of relative  
 245 edge vectors:

$$\begin{aligned} \mathbf{V}_{c, l}^{ij, L=0} &= w_{c, l} \left( L_N \left( \mathbf{x}^{ij, L=0} \right) \right) \mathbf{Y}_l^{ij} \\ \mathbf{e}_{c, l}^{ij, L=0} &= w_{c, l} \left( \mathbf{x}^{ij, L=0} \right) \mathbf{Y}_l^{ij} \end{aligned} \quad (9)$$

248 Here, the weights are learned from the initialized scalar hidden features  $\mathbf{x}^{ij, L=0}$ . Layer normaliza-  
 249 tion  $L_N$  ensures that the hidden tensor features have a balanced amplitude of each edge. The initial  
 250 node features are then computed as linear transformations of the aggregated edge features:  
 251

$$\mathbf{n}_{c, l}^{i, L=0} = \text{Linear} \left( \frac{1}{\sqrt{N_{\text{avg}}}} \sum_{j \in \mathcal{N}(i)} \mathbf{e}_{c, l}^{ij, L=0} \right) \quad (10)$$

252 Here  $\mathcal{N}(i)$  and  $N_{\text{avg}}$  are the neighbouring atoms and the average number of neighbours of atom  $-i$ .

#### 257 3.3.2 SPEED UP TENSOR PRODUCT

259 To integrate the information from the equivariant features, the tensor product is employed in all  
 260 updating blocks of the SLEM model. Generally, the tensor product in SLEM is performed with the  
 261 concatenated equivariant features  $\tilde{\mathbf{f}}_{c, l}^{ij}$  and the weighted projection of the edge shift vector  $\mathbf{r}_{ij} =$   
 262  $\mathbf{r}_i - \mathbf{r}_j$  on the spherical harmonics function  $\mathbf{Y}_l^{ij}$ . Formally:

$$\mathbf{f}_{c_3, l_3}^{ij} = \tilde{\mathbf{f}}_{c_1, l_1}^{ij} \otimes w_{c_2, l_2}^{ij} \mathbf{Y}_l^{ij} = \sum_{c_1, l_1, l_2} \tilde{w}_{c_1, l_1, l_2}^{ij} \sum_{m_1, m_2} C_{(l_1, m_1)(l_2, m_2)}^{(l_3, m_3)} f_{c_1, l_1, m_1}^{ij} Y_{l_2, m_2}^{ij} \quad (11)$$

266 Here,  $\tilde{w}_{c_1, l_1, l_2}^{ij} = \sum_{c_2} w_{c_1, c_2, l_1, l_2} w_{c_2, l_2}^{ij}$  are edge-specific parameters for each tensor product oper-  
 267 ation. Performing such tensor products on high-order features is computationally intensive. There-  
 268 fore, we applied the recently developed SO(2) Passaro & Zitnick (2023) convolution to reduce the  
 269 computation and storage complexity from  $O(l_{\max}^6)$  to  $O(l_{\max}^3)$  which we refer to the appendix.

270 3.3.3 HIDDEN UPDATES  
271

272 To construct many-body interactions, as in Fig. 2(b), the node features  $\mathbf{n}_{c,l}^i$  and hidden tensor fea-  
273 tures  $\mathbf{V}_{c,l}^{ij}$  would be concatenated and doing tensor product with the projection coefficients of edge  
274 shift vector  $\mathbf{r}_{ij}$  on the spherical harmonics functions. The operation is written formally as:  
275

$$\tilde{\mathbf{V}}_{c_3,l_3}^{ij,L} = (\mathbf{n}^{i,L-1} \parallel \mathbf{V}^{ij,L-1})_{c_1,l_1} \otimes w_{c_2,l_2}^{ij,L} \mathbf{Y}_{l_2}^{ij} \quad (12)$$

278 Unlike most MPNN, the hidden states  $\mathbf{x}^{ij}$  and  $\mathbf{V}_{c,l}^{ij}$  in SLEM depend only on the local environment  
279 of centre atom  $i$ , the shift vector  $\mathbf{r}_{ij}$ , and the atomic type and coordinate informations of atom  $j$ .  
280 Such a design excludes neighbours of  $j$  into hidden states.

281 After the tensor production, the output features  $\tilde{\mathbf{V}}_{c,l}^{ij,L}$  will be passed through the gated non-linearity  
282 Batzner et al. (2022), and transformed by an ‘‘E3linear’’ Geiger & Smidt (2022) layer to mix up the  
283 information across different channels. The new hidden feature will be multiplied by the weights  
284 learned from normalized scalar features to explicitly include the radial information and return as the  
285 updated feature  $\mathbf{V}_{c,l}^{ij,L}$ . The scalar hidden features are updated by mixing the 0th order information  
286 from  $\mathbf{V}_{c,l}^{ij,L}$  with a latent MLP, which is:  
287

$$\mathbf{x}^{ij,L} = \text{MLP}(\mathbf{x}^{ij,L-1} \parallel \mathbf{V}_{c,l=0}^{ij,L}) \cdot u(r_{ij}) \quad (13)$$

290 The scalar hidden states  $\mathbf{x}^{ij,L}$  incorporate an explicit decaying envelope function  $u(r_{ij})$  and many-  
291 body interactions of scalar and tensor features. This formulation effectively captures the decay  
292 behavior of each edge irrep feature as a function of radial distance.  
293

294 3.3.4 NODE UPDATES  
295

296 The strict local node representation  $\mathbf{n}_{c,l}^{ij,L}$  can be constructed naturally from the many-body interac-  
297 tive tensor features  $\mathbf{V}_{c,l}^{ij,L}$ . We follow the MPNN style to create the message from node  $j$  to node  $i$ .  
298 Formally:

$$\mathbf{m}_{c_3,l_3}^{ij,L} = (\mathbf{n}^{i,L-1} \parallel \mathbf{V}^{ij,L})_{c_1,l_1} \otimes w_{c_2,l_2}^{ij,L} \mathbf{Y}_{l_2}^{ij} \quad (14)$$

301 Here again, we exclude the neighbouring information of atom  $j$  in  $\mathbf{m}_{c_3,l_3}^{ij,L}$  via the partial updates  
302 of  $\mathbf{V}_{c,l}^{ij,L}$ , while maintaining necessary interactions. Each message then is passed through a gated  
303 activation and E3Linear layer, weighted separately by weights learnt from the hidden scalar features,  
304 and aggregated to update the node feature by:  
305

$$\mathbf{n}_{c_3,l_3}^{ij,L} = \alpha \cdot \mathbf{n}_{c_3,l_3}^{ij,L-1} + \frac{\sqrt{1-\alpha^2}}{N_{avg}} \sum_{j \in \mathcal{N}(i)} w_{c_3,l_3}^{ij} \mathbf{m}_{c_3,l_3}^{ij,L} \quad (15)$$

309 Here  $\alpha$  ranged from 0 to 1. The weights here differ from those in hidden updates as they are directly  
310 learnt from  $\mathbf{x}^{ij,L}$  without normalization. Therefore, the absolute radial decay is enforced in the  
311 weights, providing a strong prior that the messages from atoms at shorter distances are generally  
312 more significant. Meanwhile, the update of  $\mathbf{x}^{ij,L}$ , and consequently  $w_{c_3,l_3}^{ij}$ , depends on the features  
313  $\mathbf{V}^{ij,L}$  and  $\mathbf{n}^{i,L-1}$ , as shown in Eq.13. This structure aligns with the equivariant graph attention  
314 mechanism Liao & Smidt (2022); Liao et al. (2023) which has demonstrated powerful expressibility  
315 in various tasks. Here  $w_{c_3,l_3}^{ij}$  corresponding to an attention score computed from  $\mathbf{V}^{ij,L}$  and  $\mathbf{n}^{i,L-1}$ .  
316 Therefore, through this update, the dependencies of node features are strictly local.  
317

318 3.3.5 EDGE UPDATES  
319

320 The locality of edge features  $\mathbf{e}_{c,l}^{ij,L}$  can be naturally preserved as long as the node features are strictly  
321 local. By mixing the information of node features on both sides, localized edge updates can be  
322 formulated as follows:  
323

$$\tilde{\mathbf{e}}_{c_3,l_3}^{ij,L} = (\mathbf{n}^{i,L-1} \parallel \mathbf{V}^{ij,L} \parallel \mathbf{n}^{j,L-1})_{c_1,l_1} \otimes w_{c_2,l_2}^{ij,L} \mathbf{Y}_{l_2}^{ij} \quad (16)$$

324  
 325 Table 1: MAE (in meV) for Hamiltonian matrix predictions using SLEM and other methods on  
 326 materials with LCAO basis up to  $d$  orbitals. Numbers in parentheses indicate parameter count.

Material	Systems with LCAO-basis up to $d$ -orbitals			
	SLEM (0.7M)	SLEM (4.5M)	DeepH-E3 (1.0 M)	HamGNN (2.8M)
MoS <sub>2</sub>	<b>0.34</b>	<b>0.14</b>	0.46	0.55
Graphene	<b>0.26</b>	<b>0.14</b>	0.40	0.28
Si(300K)	<b>0.10</b>	<b>0.07</b>	0.16	0.10

331  
 332  
 333  
 334 Table 2: MAE (in meV) for Hamiltonian matrix predictions using SLEM and DeepH-E3 models  
 335 Gong et al. (2023) on materials with LCAO basis up to  $f$  and  $g$  orbitals. Numbers in parentheses  
 336 indicate parameter count. The MAE of HfO<sub>2</sub> in DeepH-E3 is absent due to out-of-memory errors.

Material	Systems with LCAO-basis up to $f$ and $g$ -orbitals	
	SLEM (1.7M)	DeepH-E3 (1.9M)
GaN	<b>0.21</b>	0.87
HfO <sub>2</sub>	<b>0.28</b>	-

347  
 348  
 349  
 350 Similarly, the updated edge features are processed via a gated activation and an E3Linear layer, and  
 351 then multiplied with weights learnt from the hidden scalar features (without normalization) as:

$$\mathbf{e}_{c_3, l_3}^{ij, L} = \alpha \cdot \mathbf{e}_{c_3, l_3}^{ij, L-1} + \sqrt{1 - \alpha^2} \cdot w_{c_3, l_3}^{ij} \tilde{\mathbf{e}}_{c_3, l_3}^{ij, L} \quad (17)$$

354  
 355 The following section focuses on validating the effectiveness of this framework via learning equiv-  
 356 ariant DFT Hamiltonians, density matrices and overlap.

## 4 RESULTS

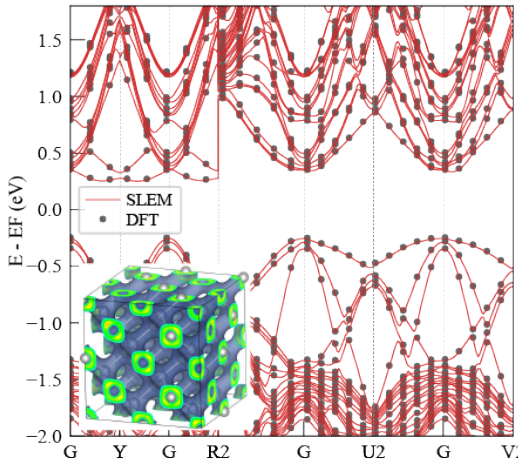
### 4.1 BENCHMARK THE ACCURACY AND DATA-EFFICIENCY

360 We evaluate our model’s performance in fitting Hamiltonian, density matrix, and overlap matrix us-  
 361 ing diverse datasets. For Hamiltonian, we use systems with up to  $d$  orbitals, including 2D systems  
 362 of monolayer MoS<sub>2</sub> and graphene from existing datasets Li et al. (2022), as well as 3D bulk silicon  
 363 generated for this study. To test SLEM’s capability with high-order tensors, we also train the models  
 364 on generated datasets of bulk GaN and HfO<sub>2</sub> systems, which include  $f$  and  $g$  orbitals. Structures in  
 365 the Si, GaN, and HfO<sub>2</sub> systems are sampled via molecular dynamics using neural network poten-  
 366 tentials Wang et al. (2018). For density matrix and overlap matrix evaluations, we focus exclusively  
 367 on the datasets of Si, GaN, and HfO<sub>2</sub> datasets, as the reported datasets for MoS<sub>2</sub> and graphene lack  
 368 density and overlap matrix data. Our model supports an atom-specific  $r_{cut}$  setting, each value cor-  
 369 responding to the radial basis cutoff of the numerical atomic orbitals, which aligns with the setting  
 370 in the compared method.

371  
 372 Table 1 presents a comparison of mean absolute error (MAE) values in Hamiltonian prediction for  
 373 graphene, MoS<sub>2</sub>, and Si systems, whose LCAO basis extends up to  $d$  orbitals, among the SLEM,  
 374 DeepH-E3 Gong et al. (2023), and HamGNN Zhong et al. (2023) methods. Our SLEM model  
 375 achieves state-of-the-art accuracy, exhibiting the lowest MAE across all systems. Notably, this high  
 376 accuracy is achieved with a relatively small model size of only 0.7 million (M) trainable parameters.  
 377 Furthermore, we extended our comparison between the SLEM and DeepH-E3 methods to include  
 378 GaN and HfO<sub>2</sub> systems, where the LCAO basis extends up to  $f$  and  $g$  orbitals, respectively. As

378  
 379 Table 3: MAE for predicting density matrix using SLEM on materials with LCAO basis up to  $d$ ,  $f$ ,  
 380 and  $g$  orbitals. Model settings align with those in Table 1.

Materials	SLEM density matrix model		
	Silicon	GaN	HfO <sub>2</sub>
	MAE	8.9e-5	2.3e-5



402  
 403 Figure 3: Comparison of band structures for a Si MD trajectory snapshot: SLEM prediction vs.  
 404 DFT calculation. Predicted band structures are obtained from either diagonalization of the predicted  
 405 Hamiltonian or NSCF DFT calculation using predicted charge density, yielding indistinguishable  
 406 results. Inset: Visualization of charge density distribution for the same structure.

407  
 408 shown in Table 2, the SLEM model consistently presents the lowest MAE, further demonstrating  
 409 its high accuracy and versatility across different orbital complexities. Fig. 3 illustrates the band  
 410 structure of silicon structures computed directly from the SLEM-predicted Hamiltonian, where the  
 411 eigenvalues are indistinguishable from those obtained using DFT. For the density matrix, fitting re-  
 412 sults are presented in Table 3. The results demonstrate very high accuracy (order of 1e-5), approach-  
 413 ing the machine precision limit of float32 numbers. In Fig. 3, we use the trained model to predict  
 414 the density matrix and visualize its real-space distribution. This capability is particularly important  
 415 for applications such as charge distribution analysis or tracking electron transfer. Furthermore, the  
 416 predicted density can be directly used for non-self-consistent field (NSCF) DFT calculations. The  
 417 resulting band structure for silicon, as an example, is highly accurate and matches the DFT output,  
 418 with a MAE of only 1.09 meV in eigenvalues compared to self-consistent DFT results. The overlap  
 419 matrix, represented by invariant SK parameters in our SLEM model, achieves exceptionally high  
 420 accuracy as demonstrated in Table 4, approaching the machine precision limit for float32 numbers.  
 421 Notably, our simplified parameterization enables this high accuracy with only a minimal increase  
 422 in model complexity. For instance, in a silicon model designed to fit only the Hamiltonian, our  
 423 typical parameter count is 0.7 M. The inclusion of overlap matrix prediction adds merely 0.01 M  
 424 parameters, which is about 1.4% in total model size.

425 Additionally, the strict localization scheme of our SLEM model confers superior data efficiency,  
 426 requiring fewer DFT-calculated data points for training. To quantify this efficiency, we conducted  
 427 an experiment using randomly split subsets of the original data, comprising 20%, 40%, 60%, and  
 428 80% of the full training set. We trained both the SLEM model and DeepH-E3 method on these  
 429 subsets and evaluated their performance on consistent validation sets. Results in table 5 demon-  
 430 strate SLEM’s high accuracy across all subsets, thus highlighting its remarkable data efficiency. This  
 431 data efficiency implies that SLEM users can generate smaller, more cost-effective training sets.  
 Moreover, SLEM’s excellent data efficiency and transferability make it particularly well-suited as a  
 backbone for developing universal DFT models, especially for systems involving heavy elements.

432  
 433 Table 4: MAE for predicting overlap matrix using SLEM’s parameterization on materials with  
 434 LCAO basis up to  $d$ ,  $f$ , and  $g$  orbitals. Model settings align with those in Table 1.

SLEM overlap prediction			
Materials	Silicon	GaN	HfO <sub>2</sub>
MAE	5.6e-5	4.7e-5	6.3e-5

439  
 440  
 441 Table 5: Comparison of validation MAE (in meV) for SLEM model and DeepH-E3 Gong et al.  
 442 (2023) method trained on randomly split datasets Li et al. (2022) with varying training ratios. Model  
 443 settings align with those in Table 1.

MoS2					
Partition	100%	80%	60%	40%	20%
SLEM	<b>0.34</b>	<b>0.37</b>	<b>0.39</b>	<b>0.37</b>	<b>0.37</b>
DeePH-E3	0.46	0.72	0.84	1.03	1.46
Graphene					
Partition	100%	80%	60%	40%	20%
SLEM	<b>0.26</b>	<b>0.26</b>	<b>0.27</b>	<b>0.21</b>	<b>0.26</b>
DeePH-E3	0.40	0.30	0.33	0.36	0.60

## 454 455 456 4.2 EFFICIENCY AND SCALABILITY

457  
 458 In materials science, chemistry, and biology, many significant properties emerge in systems con-  
 459 taining heavy atoms. These heavy atoms introduce high-order spherical tensors when represent-  
 460 ing quantum operators. Scaling to such systems is challenging due to the computational complexity  
 461 of tensor products used to construct complex spherical tensors, which scales as  $O(l^6)$ . Conven-  
 462 tional tensor production methods struggle with training and inference on systems containing heavy  
 463 atoms, making it difficult to model these important phenomena efficiently. Moreover, inferring large  
 464 material systems while training with small structures is particularly valuable, which requires par-  
 465 allelising the model inference by assigning partitions of the large atomic structure to multiple GPU  
 466 workers. However, most current models struggle with this task. As the receptive fields expand  
 467 through iterative graph updates, the minimum size of each partitioned subgraph increases, reducing  
 468 the effectiveness of such partitioning. The SLEM model addresses these challenges by efficiently  
 469 constructing high-order tensor products and assisting parallelization through its strict locality.

470 For efficiency, the implementation of SO(2) convolution reduces the tensor product computational  
 471 complexity from  $O(l^6)$  to  $O(l^3)$ , which is then further reduced by the parallelization of matrix  
 472 operations to nearly  $O(l)$  benefiting from PyTorch. Figure 4 compares the wall time and GPU  
 473 memory consumed by tensor product operations using SO(2) convolution versus the conventional  
 474 method employed in DeepH-E3 Gong et al. (2023) and E3NN Geiger & Smidt (2022). The SO(2)  
 475 convolution approach demonstrates markedly superior efficiency, enabling our method to handle all  
 476 possible basis choices in LCAO DFT. We also evaluated memory usage and training time for typical  
 477 systems, comparing our model with DeepH-E3. The results, displayed in Fig. 5, show that our model  
 478 consistently outperforms in both metrics. Notably, the advantage becomes more pronounced as the  
 479 basis set size increases, highlighting our method’s scalability. Additionally, the SLEM model’s strict  
 480 locality design significantly enhances parallelization. This localized approach allows for the division  
 481 of the atomic graph into sub-graphs, enabling independent computation of node and edge features  
 482 on separate devices. This is extremely important when expanding DFT simulation to large systems.  
 483 In practice, for HfO<sub>2</sub> with  $4s2p2d2f1g$  basis, a typical model of 1.7M parameters can predict the  
 484 quantum operators for up to  $10^3$  atoms on devices with 32GB memory. Despite linear scaling,  
 485 the inference on a system with  $10^4 \sim 10^7$  would require over 300 GB of memory, necessitating  
 486 parallelization across multiple GPUs. Therefore, a strictly localized model such as SLEM holds  
 487 significant potential for expanding simulation system sizes.

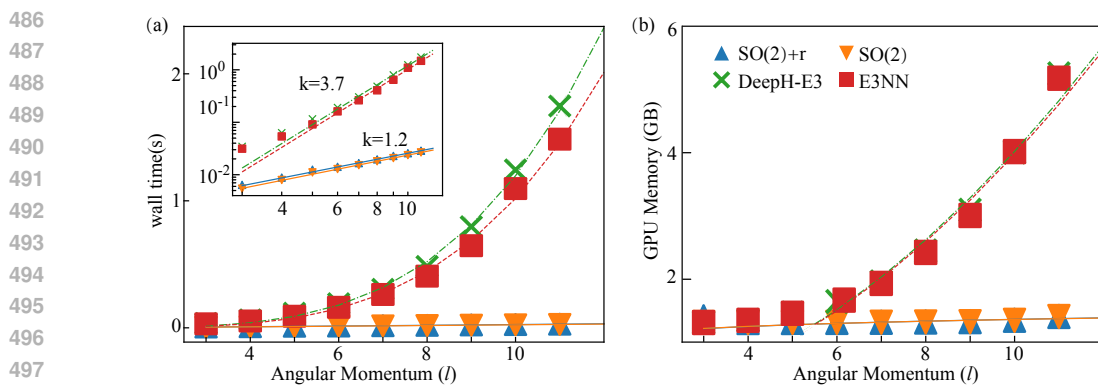


Figure 4: Comparison of time and memory consumption for different tensor-product implementations. (a) Time consumption vs. angular momentum ( $l$ ) for different models, including the SO(2)-based SLEM model (triangles) with and without radial part ( $r$ ), DeepH-E3 (cross) Gong et al. (2023), and E3NN (square) Geiger & Smidt (2022) models. Inset: Log-scale fit with slopes of 1.2 for the SLEM model and 3.7 for the other two models. (b) Memory consumption vs.  $l$ . The SLEM model demonstrates over two orders of magnitude improvement in both time and memory efficiency compared to DeepH-E3 and E3NN.

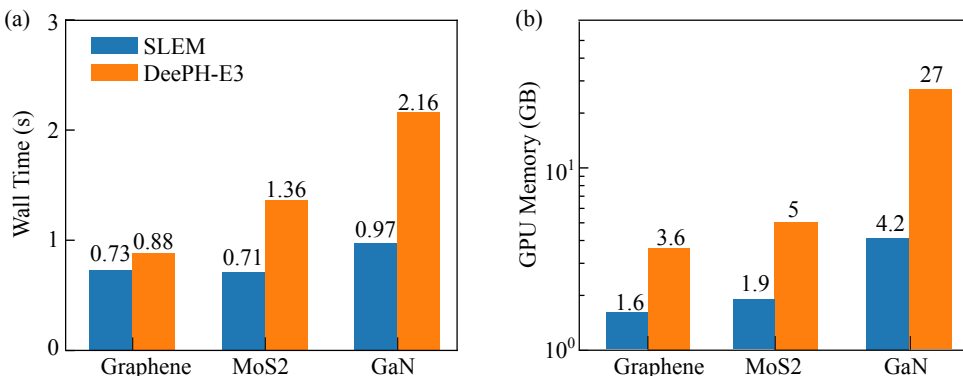


Figure 5: Comparison of training time per iteration and memory consumption with SLEM and DeepH-E3 Gong et al. (2023) models.

## 5 CONCLUSION

This work presents SLEM (Strictly Local Equivariant Message-passing) model, a novel approach for predicting quantum operator representations in materials science. By employing a strict locality design and integrating SO(2) convolution, SLEM achieves state-of-the-art performance in predicting Hamiltonians, density matrices, and overlap matrices for diverse materials, including systems with heavy atoms. The model’s efficiency and scalability open new possibilities for large-scale quantum simulations and high-throughput materials discovery. Notably, SLEM’s locality enables efficient parallelization through atomic graph partitioning, potentially extending its applicability to extremely large systems at device-level scales. SLEM’s intrinsic support for multiple quantum operators, coupled with its novel overlap matrix parameterization, significantly reduces computational costs and dependence on post-training DFT software. The model demonstrates superior data efficiency and transferability, making it particularly well-suited for developing universal DFT models, especially for systems involving heavy elements. These advancements position SLEM as a powerful tool for simulating complex systems in materials science and computational chemistry. Looking ahead, future work will focus on developing robust sampling methodologies for active learning and integrating SLEM with existing software ecosystems to fully leverage its capabilities in real-world applications, further advancing the field of computational materials science.

540 REFERENCES  
541

- 542 Albert P. Bartók, Mike C. Payne, Risi Kondor, and Gábor Csányi. Gaussian approximation potentials:  
543 The accuracy of quantum mechanics, without the electrons. *Phys. Rev. Lett.*, 104:136403,  
544 Apr 2010. doi: 10.1103/PhysRevLett.104.136403. URL <https://link.aps.org/doi/10.1103/PhysRevLett.104.136403>.
- 545 Ilyes Batatia, David P Kovacs, Gregor Simm, Christoph Ortner, and Gábor Csányi.  
546 MACE: Higher order equivariant message passing neural networks for fast and accu-  
547 rate force fields. *Advances in Neural Information Processing Systems*, 35:11423–11436,  
548 2022. URL [https://proceedings.neurips.cc/paper\\_files/paper/2022/file/4a36c3c51af11ed9f34615b81edb5bbc-Paper-Conference.pdf](https://proceedings.neurips.cc/paper_files/paper/2022/file/4a36c3c51af11ed9f34615b81edb5bbc-Paper-Conference.pdf).
- 549 Simon Batzner, Albert Musaelian, Lixin Sun, Mario Geiger, Jonathan P Mailoa, Mordechai Korn-  
550 bluth, Nicola Molinari, Tess E Smidt, and Boris Kozinsky. E(3)-equivariant graph neural networks  
551 for data-efficient and accurate interatomic potentials. *Nature Communications*, 13(1):2453, 2022.  
552 URL <https://doi.org/10.1038/s41467-022-29939-5>.
- 553 Jörg Behler and Michele Parrinello. Generalized neural-network representation of high-dimensional  
554 potential-energy surfaces. *Phys. Rev. Lett.*, 98:146401, Apr 2007. doi: 10.1103/PhysRevLett.98.  
555 146401. URL <https://link.aps.org/doi/10.1103/PhysRevLett.98.146401>.
- 556 Xinyang Dong, Emanuel Gull, and Lei Wang. Equivariant neural network for green's functions  
557 of molecules and materials. *Phys. Rev. B*, 109:075112, Feb 2024. doi: 10.1103/PhysRevB.109.  
558 075112. URL <https://link.aps.org/doi/10.1103/PhysRevB.109.075112>.
- 559 Matthias Ernzerhof and Gustavo E Scuseria. Assessment of the perdew–burke–ernzerhof exchange-  
560 correlation functional. *The Journal of chemical physics*, 110(11):5029–5036, 1999.
- 561 Mario Geiger and Tess Smidt. e3nn: Euclidean neural networks. *arXiv:2207.09453*, 2022. URL  
562 <https://arxiv.org/abs/2207.09453>.
- 563 Justin Gilmer, Samuel S Schoenholz, Patrick F Riley, Oriol Vinyals, and George E Dahl. Neural mes-  
564 sage passing for quantum chemistry. In *International conference on machine learning*, pp. 1263–  
565 1272. PMLR, 2017. URL <https://dl.acm.org/doi/10.5555/3305381.3305512>.
- 566 Xiaoxun Gong, He Li, Nianlong Zou, Runzhang Xu, Wenhui Duan, and Yong Xu. General frame-  
567 work for E(3)-equivariant neural network representation of density functional theory Hamiltonian.  
568 *Nature Communications*, 14(1):2848, 2023. URL <https://doi.org/10.1038/s41467-023-38468-8>.
- 569 Qiangqiang Gu, Zhanghao Zhouyin, Shishir Kumar Pandey, Peng Zhang, Linfeng Zhang, and  
570 Weinan E. DeePTB: A deep learning-based tight-binding approach with *ab initio* accuracy.  
571 *arXiv:2307.04638*, 2023. URL <https://arxiv.org/abs/2307.04638>.
- 572 DR Hamann. Optimized norm-conserving vanderbilt pseudopotentials. *Physical Review  
573 B—Condensed Matter and Materials Physics*, 88(8):085117, 2013.
- 574 Jiaqi Han, Jiacheng Cen, Liming Wu, Zongzhao Li, Xiangzhe Kong, Rui Jiao, Ziyang Yu, Tingyang  
575 Xu, Fandi Wu, Zihe Wang, et al. A survey of geometric graph neural networks: Data structures,  
576 models and applications. *arXiv:2403.00485*, 2024. URL <https://arxiv.org/abs/2403.00485>.
- 577 P. Hohenberg and W. Kohn. Inhomogeneous electron gas. *Phys. Rev.*, 136:B864–B871, Nov  
578 1964. doi: 10.1103/PhysRev.136.B864. URL <https://link.aps.org/doi/10.1103/PhysRev.136.B864>.
- 579 E Huckel and P Debye. Zur theorie der elektrolyte. i. gefrierpunktserniedrigung und verwandte  
580 erscheinungen. *Phys. Z.*, 24:185–206, 1923.
- 581 Simão M João, Miša Anelović, Lucian Covaci, Tatiana G Rappoport, João MVP Lopes, and Aires  
582 Ferreira. Kite: high-performance accurate modelling of electronic structure and response func-  
583 tions of large molecules, disordered crystals and heterostructures. *Royal Society Open Science*,  
584 7(2):191809, 2020. URL <https://royalsocietypublishing.org/doi/abs/10.1098/rsos.191809>.

- 594 R. O. Jones. Density functional theory: Its origins, rise to prominence, and future. *Rev. Mod. Phys.*,  
 595 87:897–923, Aug 2015. doi: 10.1103/RevModPhys.87.897. URL <https://link.aps.org/doi/10.1103/RevModPhys.87.897>.
- 596
- 597 Chaitanya K Joshi, Cristian Bodnar, Simon V Mathis, Taco Cohen, and Pietro Lio. On the expressive  
 598 power of geometric graph neural networks. In *International conference on machine learning*, pp. 15330–15355. PMLR, 2023. URL <https://proceedings.mlr.press/v202/joshi23a/joshi23a.pdf>.
- 599
- 600
- 601
- 602 W. Kohn and L. J. Sham. Self-consistent equations including exchange and correlation effects.  
 603 *Phys. Rev.*, 140:A1133–A1138, Nov 1965. doi: 10.1103/PhysRev.140.A1133. URL <https://link.aps.org/doi/10.1103/PhysRev.140.A1133>.
- 604
- 605 Risi Kondor. N-body networks: a covariant hierarchical neural network architecture for learning  
 606 atomic potentials. *arXiv:1803.01588*, 2018. URL <https://arxiv.org/abs/1803.01588>.
- 607
- 608
- 609 Risi Kondor, Zhen Lin, and Shubhendu Trivedi. Clebsch–Gordan nets: a fully fourier space  
 610 spherical convolutional neural network. *Advances in Neural Information Processing Systems*,  
 611 31, 2018. URL [https://proceedings.neurips.cc/paper\\_files/paper/2018/file/a3fc981af450752046be179185ebc8b5-Paper.pdf](https://proceedings.neurips.cc/paper_files/paper/2018/file/a3fc981af450752046be179185ebc8b5-Paper.pdf).
- 612
- 613 He Li, Zun Wang, Nianlong Zou, Meng Ye, Runzhang Xu, Xiaoxun Gong, Wenhui Duan, and Yong  
 614 Xu. Deep-learning density functional theory hamiltonian for efficient ab initio electronic-structure  
 615 calculation. *Nature Computational Science*, 2(6):367–377, 2022. URL <https://doi.org/10.1038/s43588-022-00265-6>.
- 616
- 617 Pengfei Li, Xiaohui Liu, Mohan Chen, Peize Lin, Xinguo Ren, Lin Lin, Chao Yang, and Lixin He.  
 618 Large-scale ab initio simulations based on systematically improvable atomic basis. *Computational  
 619 Materials Science*, 112:503–517, 2016.
- 620
- 621 Yunhai Li, Zhen Zhan, Xueheng Kuang, Yonggang Li, and Shengjun Yuan. TBPLaS: A tight-  
 622 binding package for large-scale simulation. *Computer Physics Communications*, 285:108632,  
 623 April 2023. ISSN 0010-4655. doi: 10.1016/j.cpc.2022.108632.
- 624
- 625 Yi-Lun Liao and Tess Smidt. Equiformer: Equivariant graph attention transformer for 3d atomistic  
 626 graphs. *arXiv:2206.11990*, 2022. URL <https://arxiv.org/abs/2206.11990>.
- 627
- 628 Yi-Lun Liao, Brandon Wood, Abhishek Das, and Tess Smidt. EquiformerV2: Improved equivariant  
 629 transformer for scaling to higher-degree representations. *arXiv:2306.12059*, 2023. URL <https://arxiv.org/abs/2306.12059>.
- 630
- 631 Albert Musaelian, Simon Batzner, Anders Johansson, Lixin Sun, Cameron J. Owen, Mordechai  
 632 Kornbluth, and Boris Kozinsky. Learning local equivariant representations for large-scale atom-  
 633 istic dynamics. *Nature Communications*, 14(1):579, February 2023. ISSN 2041-1723. doi:  
 634 10.1038/s41467-023-36329-y.
- 635
- 636 Jigyasa Nigam, Michael J. Willatt, and Michele Ceriotti. Equivariant representations for molecular  
 637 Hamiltonians and N-center atomic-scale properties. *The Journal of Chemical Physics*, 156(1):  
 014115, 01 2022. ISSN 0021-9606. doi: 10.1063/5.0072784. URL <https://doi.org/10.1063/5.0072784>.
- 638
- 639 D. Ninno, F. Trani, G. Cantele, K. J. Hameeuw, G. Iadonisi, E. Degoli, and S. Ossicini. Thomas-  
 640 Fermi model of electronic screening in semiconductor nanocrystals. *Europhysics Letters*, 74(3):  
 641 519, mar 2006. doi: 10.1209/epl/i2005-10544-9. URL <https://dx.doi.org/10.1209/epl/i2005-10544-9>.
- 642
- 643 Saro Passaro and C Lawrence Zitnick. Reducing SO(3) convolutions to SO(2) for efficient equiv-  
 644 ariant gnns. In *International Conference on Machine Learning*, pp. 27420–27438. PMLR, 2023.  
 645 URL <https://dl.acm.org/doi/10.5555/3618408.3619548>.
- 646
- 647 A. V. Podolskiy and P. Vogl. Compact expression for the angular dependence of tight-binding  
 648 Hamiltonian matrix elements. *Phys. Rev. B*, 69:233101, Jun 2004. doi: 10.1103/PhysRevB.69.  
 649 233101. URL <https://link.aps.org/doi/10.1103/PhysRevB.69.233101>.

- 648 Raghunathan Ramakrishnan, Pavlo O Dral, Matthias Rupp, and O Anatole Von Lilienfeld. Quantum  
 649 chemistry structures and properties of 134 kilo molecules. *Scientific data*, 1(1):1–7, 2014.  
 650
- 651 Raffaele Resta. Thomas-fermi dielectric screening in semiconductors. *Phys. Rev. B*, 16:2717–  
 652 2722, Sep 1977. doi: 10.1103/PhysRevB.16.2717. URL <https://link.aps.org/doi/10.1103/PhysRevB.16.2717>.
- 653
- 654 Lars Ruddigkeit, Ruud Van Deursen, Lorenz C Blum, and Jean-Louis Reymond. Enumeration of 166  
 655 billion organic small molecules in the chemical universe database gdb-17. *Journal of chemical  
 656 information and modeling*, 52(11):2864–2875, 2012.
- 657
- 658 Víctor Garcia Satorras, Emiel Hoogeboom, and Max Welling. E(n) equivariant graph neural net-  
 659 works. In *International conference on machine learning*, pp. 9323–9332. PMLR, 2021. URL  
 660 <https://proceedings.mlr.press/v139/satorras21a/satorras21a.pdf>.
- 661
- 662 K. T. Schütt, H. E. Sauceda, P.-J. Kindermans, A. Tkatchenko, and K.-R. Müller. SchNet – A deep  
 663 learning architecture for molecules and materials. *The Journal of Chemical Physics*, 148(24):  
 664 241722, 03 2018. ISSN 0021-9606. doi: 10.1063/1.5019779. URL <https://doi.org/10.1063/1.5019779>.
- 665
- 666 Kristof T Schütt, Stefan Chmiela, O Anatole Von Lilienfeld, Alexandre Tkatchenko, Koji Tsuda,  
 667 and Klaus-Robert Müller. Machine learning meets quantum physics. *Lecture Notes in Physics*,  
 668 2020.
- 669
- 670 Guillen Simeon and Gianni De Fabritiis. TensorNet: Cartesian tensor representations for efficient  
 671 learning of molecular potentials. *Advances in Neural Information Processing Systems*, 36, 2024.  
 672 URL <https://openreview.net/forum?id=BH1PdBZ2e>.
- 673
- 674 J. C. Slater and G. F. Koster. Simplified LCAO method for the periodic potential problem. *Phys.  
 675 Rev.*, 94:1498–1524, Jun 1954. doi: 10.1103/PhysRev.94.1498. URL <https://link.aps.org/doi/10.1103/PhysRev.94.1498>.
- 676
- 677 Nathaniel Thomas, Tess Smidt, Steven Kearnes, Lusann Yang, Li Li, Kai Kohlhoff, and Patrick  
 678 Riley. Tensor field networks: Rotation-and translation-equivariant neural networks for 3d point  
 679 clouds. *arXiv:1802.08219*, 2018. URL <https://arxiv.org/abs/1802.08219>.
- 680
- 681 Aidan P Thompson, H Metin Aktulga, Richard Berger, Dan S Bolintineanu, W Michael Brown,  
 682 Paul S Crozier, Pieter J In’t Veld, Axel Kohlmeyer, Stan G Moore, Trung Dac Nguyen, et al.  
 683 Lammmps-a flexible simulation tool for particle-based materials modeling at the atomic, meso, and  
 684 continuum scales. *Computer Physics Communications*, 271:108171, 2022.
- 685
- 686 A.P. Thompson, L.P. Swiler, C.R. Trott, S.M. Foiles, and G.J. Tucker. Spectral neighbor analysis  
 687 method for automated generation of quantum-accurate interatomic potentials. *Journal of Com-  
 688 putational Physics*, 285:316–330, 2015. ISSN 0021-9991. doi: <https://doi.org/10.1016/j.jcp.2014.12.018>. URL <https://www.sciencedirect.com/science/article/pii/S0021999114008353>.
- 689
- 690 Oliver Unke, Mihail Bogojeski, Michael Gastegger, Mario Geiger, Tess Smidt, and Klaus-  
 691 Robert Müller. SE(3)-equivariant prediction of molecular wavefunctions and elec-  
 692 tronic densities. *Advances in Neural Information Processing Systems*, 34:14434–  
 693 14447, 2021. URL <https://proceedings.neurips.cc/paper/2021/file/78f1893678afbeaa90b1fa01b9cfb860-Paper.pdf>.
- 694
- 695 Jonathan Vandermause, Steven B. Torrisi, Simon Batzner, Yu Xie, Lixin Sun, Alexie M. Kolpak,  
 696 and Boris Kozinsky. On-the-fly active learning of interpretable Bayesian force fields for atomistic  
 697 rare events. *npj Computational Materials*, 6(1):1–11, March 2020. ISSN 2057-3960. doi: 10.  
 698 1038/s41524-020-0283-z.
- 699
- 700 Han Wang, Linfeng Zhang, Jiequn Han, and Weinan E. DeePMD-kit: A deep learning package for  
 701 many-body potential energy representation and molecular dynamics. *Computer Physics Commu-  
 702 nications*, 228:178–184, July 2018. ISSN 0010-4655. doi: 10.1016/j.cpc.2018.03.016.

702 Maurice Weiler, Mario Geiger, Max Welling, Wouter Boomsma, and Taco S Co-  
 703 hen. 3D Steerable CNNs: Learning rotationally equivariant features in volumet-  
 704 ric data. *Advances in Neural Information Processing Systems*, 31, 2018. URL  
 705 [https://proceedings.neurips.cc/paper\\_files/paper/2018/file/488e4104520c6aab692863cc1dba45af-Paper.pdf](https://proceedings.neurips.cc/paper_files/paper/2018/file/488e4104520c6aab692863cc1dba45af-Paper.pdf).  
 706

707 Shi Yin, Xinyang Pan, Fengyan Wang, Feng Wu, and Lixin He. A framework of  $so(3)$ -equivariant  
 708 non-linear representation learning and its application to electronic-structure hamiltonian predi-  
 709 cation. *arXiv:2405.05722*, 2024. URL <https://arxiv.org/abs/2405.05722>.  
 710

711 Haiyang Yu, Zhao Xu, Xiaofeng Qian, Xiaoning Qian, and Shuiwang Ji. Efficient and equivariant  
 712 graph networks for predicting quantum hamiltonian. In *International Conference on Machine  
 713 Learning*, pp. 40412–40424. PMLR, 2023. URL <https://proceedings.mlr.press/v202/yu23i.html>.  
 714

715 Haiyang Yu, Meng Liu, Youzhi Luo, Alex Strasser, Xiaofeng Qian, Xiaoning Qian, and Shuiwang  
 716 Ji. Qh9: A quantum hamiltonian prediction benchmark for qm9 molecules. *Advances in Neural  
 717 Information Processing Systems*, 36, 2024.  
 718

719 Linfeng Zhang, Jiequn Han, Han Wang, Roberto Car, and Weinan E. Deep potential molecular dy-  
 720 namics: A scalable model with the accuracy of quantum mechanics. *Phys. Rev. Lett.*, 120:143001,  
 721 Apr 2018a. doi: 10.1103/PhysRevLett.120.143001. URL <https://link.aps.org/doi/10.1103/PhysRevLett.120.143001>.  
 722

723 Linfeng Zhang, Jiequn Han, Han Wang, Wissam Saidi, Roberto Car, and Weinan  
 724 E. End-to-end symmetry preserving inter-atomic potential energy model for finite  
 725 and extended systems. *Advances in Neural Information Processing Systems*, 31,  
 726 2018b. URL [https://proceedings.neurips.cc/paper\\_files/paper/2018/file/e2ad76f2326fbc6b56a45a56c59fafdb-Paper.pdf](https://proceedings.neurips.cc/paper_files/paper/2018/file/e2ad76f2326fbc6b56a45a56c59fafdb-Paper.pdf).  
 727

728 Yuzhi Zhang, Haidi Wang, Weijie Chen, Jinzhe Zeng, Linfeng Zhang, Han Wang, and Weinan E.  
 729 DP-GEN: A concurrent learning platform for the generation of reliable deep learning based po-  
 730 tential energy models. *Computer Physics Communications*, 253:107206, 2020. ISSN 0010-4655.  
 731 doi: <https://doi.org/10.1016/j.cpc.2020.107206>. URL <https://www.sciencedirect.com/science/article/pii/S001046552030045X>.  
 732

734 Yang Zhong, Hongyu Yu, Mao Su, Xingao Gong, and Hongjun Xiang. Transferable equivariant  
 735 graph neural networks for the hamiltonians of molecules and solids. *npj Computational Materials*,  
 736 9(1):182, 2023. URL <https://doi.org/10.1038/s41524-023-01130-4>.  
 737

Larry Zitnick, Abhishek Das, Adeesh Kolluru, Janice Lan, Muhammed Shuaibi, Anuroop  
 738 Sriram, Zachary Ulissi, and Brandon Wood. Spherical channels for modeling atomic  
 739 interactions. *Advances in Neural Information Processing Systems*, 35:8054–8067,  
 740 2022. URL [https://proceedings.neurips.cc/paper\\_files/paper/2022/file/3501bea1ac61fedbaaff2f88e5fa9447-Paper-Conference.pdf](https://proceedings.neurips.cc/paper_files/paper/2022/file/3501bea1ac61fedbaaff2f88e5fa9447-Paper-Conference.pdf).  
 741

## A BENCHMARK ON QH-9

We also train our model on the open molecule Hamiltonian and Overlap dataset, QH-9 Yu et al. (2024), to test our method’s accuracy and transferability on a large dataset. We compare our result with the reported benchmark QH-net, which shows considerable accuracy improvement, as displayed in 6. We should notice that our model performs well in the Hamiltonian learning tasks, by decreasing 1/3 of the error reported previously. The density matrix is inferred from the learned Hamiltonian since the data is not available in QH9. Our accuracy is only 1/3 of the compared one.

QH9 is an extended electronic structure dataset based on QM9 Ruddigkeit et al. (2012); Ramakrishnan et al. (2014), a well-known benchmark for molecular property prediction. QH-9 contains 13,081 static structures and 2998 molecular trajectories. We test our method based on the static out-of-distribution(OOD) tasks defined by QHnet’s paper, where the training set and testing set are

Table 6: MAE for Hamiltonian matrix (H) and density matrix (D) prediction.

QH-9 dataset benchmark				
Method	<b>H</b> [ $10^{-6} E_h$ ]			<b>D</b>
	all	non-diag	diag	all
LEM	<b>56.57</b>	<b>44.86</b>	155.24	<b>0.0219</b>
QHnet	83.22	80.26	135.63	0.0643

divided fully, where the testing set has a very different molecular structure and atom number w.r.t. training set. For OOD, the dataset is split as 104,001/17,495/9,335. As discussed in D, we used a semi-local variant of SLEM to prevent the possible break of strict locality in the molecular system.

## B ON THE STRICT LOCALITY APPROXIMATION

Here we want to further discuss the strict locality approximation made in our method. In the quantum operator learning task, we express the physical operators using an LCAO basis. In this expression, the theoretical framework of DFT fundamentally supports the strict locality approximation. In LCAO-based DFT calculations, the Hamiltonian matrix elements exhibit inherent locality. This locality manifests through two mechanisms: the spatial decay of LCAO basis functions, the electron neutralized conditions of the physics system, and electronic screening effects especially in condensed matter systems. These effects make the dependency of the quantum operator elements approximately local. For periodic systems, particularly metals and semiconductors, electronic screening effectively reduces long-range Coulomb interactions. The screening length varies by material type around 4 Å in semiconductors like silicon, and Germanium, and smaller in insulators such as 2.76 Å in Diamond. Therefore, we are safe to choose a cutoff radius to match the sum of basis orbital radii, adequately captures the correct physical relations. Taking the Hamiltonian matrix elements as an example:

$$V_{ij}^H = \int \phi_i^*(r - R_A) [V_H(r) + V_{ext}(r) + V_{xc}(r)] \phi_j(r - R_B) dr$$

The locality is a combination of the LCAO basis, Hartree term, external potential, and xc functional. Therefore, we need to discuss the localization as a collective effect, which is contributed by the following properties:

**The decaying behaviour of the LCAO basis.** For all LCAO bases (whether GTO, NAO, or Slater-like), the radial part all decays rapidly with distance. Therefore, the long-range term in  $V_H$ ,  $V_{ext}$ ,  $V_{xc}$ 's contribution in the integration (that decays as  $1/r$ ) would be decreased fastly (often exponentially such as in GTO or Slater-like orbital).

**The system's electronic neutralization condition.** The electronic neutralization condition requires that the long-term part of the Hartree term and the external term cancel each other. To derive this, we assign the electron density to the atomic center, by writing as:

$$n(r) = \sum_I n_I(r - R_I)$$

Then the sum of  $V_H(r)$ ,  $V_{ext}(r)$  would be:

$$-\sum_I \frac{Z_I}{|r - R_I|} + \sum_I \int \frac{n_I(r' - R_I)}{|r - r'|} dr'$$

When  $|r - R_I|$  is large, we can approximate  $|r - r'| \approx |r - R_I|$ , therefore:

$$-\frac{Z_I}{r - R_I} + \int \frac{n_I(r' - R_I)}{|r - r'|} dr' \approx -\frac{Z_I}{|r - R_I|} + \frac{Z_I}{|r - R_I|} = 0$$

**The screening effect.** we refer to Huckel & Debye (1923); Resta (1977); Ninno et al. (2006) the study of screening radius  $R_s$ , which describes the system’s electrostatic potential’s reaction to the vibration of charges.

In Resta (1977), the screening radius of typical insulator and semiconductor systems is reported as: Diamond: 2.76 a.u, Silicon: 4.28 a.u. and Germanium: 4.71 a.u. In Ninno et al. (2006), for some nanoparticles, the  $R_s$  is reported as: Si191H148: 5.36 a.u. and Ge191H148: 5.61 a.u.

These effects motivate us to design SLEM, as a strict localized model that is suitable to learn the correct mapping from structures to quantum operators with the correct physical priors. Consititude is a more reliable, data-efficient method. Meanwhile, we also notice the existing limitation of this method in some special systems, we refer to the discussion in D for detail.

## C COMPARISON OF SLEM WITH MPNN

**Message-passing Neural Networks** In the message-passing scheme, atoms are treated as nodes in graphs, with bonds to neighbouring atoms represented as connected edges within a specified cutoff radius. The embedded atomic features are processed by trainable functions, generating messages from each edge to update the embeddings of central atoms. Formally, the MPNN framework can be summarized as follows:

$$\begin{aligned}\mathbf{e}^{ij,L} &= \mathcal{N}_L(\mathbf{n}^{i,L-1}, \mathbf{n}^{j,L-1}, \mathbf{e}^{ij,L-1}) \\ \mathbf{m}^{ij,L} &= M_L(\mathbf{n}^{i,L-1}, \mathbf{n}^{j,L-1}, \mathbf{e}^{ij,L}) \\ \mathbf{n}^{i,L} &= U_L\left(\mathbf{n}^{i,L-1}, \sum_{j \in \mathcal{N}(i)} \mathbf{m}^{ij,L}\right)\end{aligned}$$

Here,  $\mathbf{e}^{ij,L}$  represents the edge features,  $\mathbf{m}^{ij,L}$  denotes the messages, and  $\mathbf{n}^{i,L}$  indicates the node features at layer  $L$ .  $\mathcal{N}_L$ ,  $M_L$ , and  $U_L$  are the trainable functions for the edge, message, and node updates.  $\mathcal{N}(i) = \{j | r_{ij} < r_{\text{cut}}\}$  indicates all the neighbour atoms for atom  $i$ , with  $r_{\text{cut}}$  being the predefined cutoff. This updating framework allows for the construction of many-body interactions and long-term dependencies, leading to strong performance across various applications. Here we reframe the updating rules of SLEM with the MPNN framework, which looks like this:

$$\begin{aligned}\mathbf{V}^{ij,L} &= \mathcal{V}_L(\mathbf{n}^{i,L-1}, \mathbf{V}^{ij,L-1}) \\ \mathbf{e}^{ij,L} &= \mathcal{N}_L(\mathbf{n}^{i,L-1}, \mathbf{V}^{ij,L}, \mathbf{n}^{j,L-1}, \mathbf{e}^{ij,L-1}) \\ \mathbf{m}^{ij,L} &= M_L(\mathbf{n}^{i,L-1}, \mathbf{V}^{ij,L}) \\ \mathbf{n}^{i,L} &= U_L\left(\mathbf{n}^{i,L-1}, \sum_{j \in \mathcal{N}(i)} \mathbf{m}^{ij,L}\right)\end{aligned}$$

Here  $\mathcal{V}_L$  is the neural network for hidden feature construction. This update scheme constructs many-body interactions to build equivariant edge and node features while preserving the absolute locality by excluding atoms outside the constant cutoff radius. Such a scheme, in principle, would have much better transferability, data efficiency, as well as scalability when we have a strong prior that the input and output are dependent spatially local.

## D MORE ON TENSOR PRODUCT

To integrate the information from the equivariant features, the tensor product is employed in all updating blocks of the SLEM model. Generally, the tensor product in SLEM is performed with the concatenated equivariant features  $\tilde{\mathbf{f}}_{c,l}^{ij}$  and the weighted projection of the edge shift vector  $\mathbf{r}_{ij} = \mathbf{r}_i - \mathbf{r}_j$  on the spherical harmonics function  $\mathbf{Y}_l^{ij}$ . Formally:

$$\mathbf{f}_{c_3, l_3}^{ij} = \tilde{\mathbf{f}}_{c_1, l_1}^{ij} \otimes w_{c_2, l_2}^{ij} \mathbf{Y}_l^{ij} = \sum_{c_1, l_1, l_2} \tilde{w}_{c_1, l_1, l_2}^{ij} \sum_{m_1, m_2} C_{(l_1, m_1)(l_2, m_2)}^{(l_3, m_3)} f_{c_1, l_1, m_1}^{ij} Y_{l_2, m_2}^{ij} \quad (18)$$

864 Here,  $\tilde{w}_{c_1, l_1, l_2}^{ij} = \sum_{c_2} w_{c_1, c_2, l_1, l_2} w_{c_2, l_2}^{ij}$  are edge-specific parameters for each tensor product operation. Performing such tensor products on high-order features is computationally intensive. Therefore, we applied the recently developed SO(2) Passaro & Zitnick (2023) convolution to simplify, reducing the computation and storage complexity from  $O(l_{\max}^6)$  to  $O(l_{\max}^3)$ . The simplification idea is intuitive.  $\mathbf{Y}_{l_2, m_2}^{ij}$  are sparse tensors if rotated to align with the edge  $ij$ , which is nonzero only for  $m_2 = 0$ . Therefore, it is easier to compute the tensor production in the direction of edge  $ij$ , and rotate inversely the output afterwards. This step removes the  $m_2$  index from the summation in Eq. 18. Furthermore, considering the Clebsch-Gordan coefficients with  $m_2 = 0$ , we find that  $C_{(l_1, m_1)(l_2, 0)}^{(l_3, m_3)} = 0$  except for  $m_3 = \pm m_1$ . This allows further reduction of the summation in Eq. 18 by replacing  $\pm m_1$  with a single index  $m$ . Then the operations can be reformulated formally as:

$$\begin{pmatrix} f_{c, l, m}^{ij} \\ f_{c, l, -m}^{ij} \end{pmatrix} = \sum_{c', l'} \begin{pmatrix} w_{c, c', l', m} - w_{c, c', l', -m} \\ w_{c, c', l', -m} \end{pmatrix} \cdot \begin{pmatrix} \tilde{f}_{c', l', m}^{ij} \\ \tilde{f}_{c', l', -m}^{ij} \end{pmatrix}$$

875 This represents a linear operation on  $\tilde{f}_{c', l', m}^{ij}$ . By employing this method, high-order tensor products  
 876 for  $l = 8, 9$  and even  $10$  can be efficiently calculated, which is essential for heavy element systems  
 877 where the  $f, g$  or even higher orbitals are used in the LCAO basis for DFT calculations. Finally, the  
 878 weights for the new SO(2) tensor product method are multiplied by edge-specific parameters, where  
 879  $w_{c', l'}^{ij}$  are mapped by an MLP from hidden scalar features  $\mathbf{x}^{ij, L}$  as  $\tilde{w}_{c, c', l', m}^{ij} = w_{c, c', l', m} w_{c', l'}^{ij}$ . This  
 880 powerful and efficient tensor product layer facilitates the construction of local interactive updates of  
 881 the features.

## E DATA GENERATION

890 In this section, we discuss the data generation process used in experiments of this work. The data  
 891 sampling process includes the Hamiltonian, overlap and density matrix of materials Si, GaN, HfO<sub>2</sub>.

892 First, we perform an ab-initio molecular dynamic simulation using a neural network force field using  
 893 DeePMDWang et al. (2018) and LammpsThompson et al. (2022). A typical input file of the lammps  
 894 sampling looks like:

```

896 variable      NSTEPS          equal 500000
897 variable      THERMO_FREQ    equal 100
898 variable      DUMP_FREQ     equal 1000
899 variable      TEMP           equal 300
900 variable      PRES           equal 1.00
901 variable      TAU_T          equal 0.10
902 variable      TAU_P          equal 0.50
903
904 units          metal
905 boundary       p p p
906 atom_style     atomic
907
908 neighbor        1.0 bin
909
910 read_data      conf.lammps-data
911 mass            1 28.085
912
913 pair_style      deepmd graph.pb
914 pair_coeff      * * Si
915
916 thermo_style   custom step temp pe ke etotal press vol lx ly lz xy xz yz
917 thermo          ${THERMO_FREQ}
918 restart         1000000 dpgen.restart
919
920 velocity        all create ${TEMP} 449414

```

```

918 fix           1 all nvt temp ${TEMP} ${TEMP} 0.1
919 dump          1 all custom ${DUMP_FREQ} eq.lammpstrj id type x y z vx vy vz
920
921 timestep      0.001
922
923 run           100000
924
925 undump 1
926 dump          2 all custom ${DUMP_FREQ} sample.lammpstrj id type x y z vx vy vz
927 run           ${NSTEPS} upto

```

928 The samples are taken after  $10^5$  steps when the system reaches equilibrium.

930 After the configuration sampling, we then applied ABACUSLi et al. (2016) to compute the quan-  
931 tum operators, including the Hamiltonian, density and overlap matrix of each configuration. Among  
932 them, 150 frames are randomly split as the training set, and 30 frames are used for testing. We  
933 use SG15 ONCV numerical atomic orbitals, pseudopotentialsHamann (2013), and PBE function-  
934 alsErnzerhof & Scuseria (1999) for the DFT calculation. A typical DFT calculation input looks  
935 like:

```

936 INPUT_PARAMETERS
937 # Created by Atomic Simulation Enviroment
938 ntype           1
939 ecutwfc        100
940 scf_nmax       100
941 smearing_method gaussian
942 smearing_sigma 0.002
943 basis_type     lcao
944 ks_solver      genelpa
945 mixing_type    pulay
946 mixing_beta   0.7
947 scf_thr        1e-07
948 out_chg        1
949 symmetry       1
950 calculation    scf
951 out_band       1
952 force_thr     0.001
953 out_stru       1
954 kspacing        0.08
955 lspinorb       0
956 out_wfc_lcao  0
957 dft_functional pbe
958 out_mat_hs2    True

```

959 After the calculation converged for all, we processed the data format into machine-learning read-  
960 able datasets and started training. The dataset used in this work is uploaded in the opensource  
961 platform AISquare via this link: [https://www.aissquare.com/datasets/detail?  
962 pageType=datasets&name=Quantum\\_Operator\\_Dataset&id=286](https://www.aissquare.com/datasets/detail?pageType=datasets&name=Quantum_Operator_Dataset&id=286).

## 966 F CUTOFF SELECTION

968 The cutoff used in the SLEM model is important since it decides the size of the atom and bond  
969 environment to consider when learning the map from the atomic structure to the quantum operators.  
970 There are two cutoff concepts in the SLEM model. One is the cutoff for the bond  $r_b$ , which is used  
971 to build the one-to-one correspondence of the graph structure of atomic data to the diagonal and  
off-diagonal blocks of the quantum operators. Another one is the cutoff for environment  $r_e$ .

972 For  $r_b$ , since the bond whose radial distance beyond  $r_b$  would all be considered 0, this value should  
 973 be fixed according to the LCAO orbital used in DFT data generation. For numerical atomic orbitals  
 974 (NAOs), the cutoff is defined clearly in orbital files or DFT software, therefore, we just double  
 975 (since two orbitals constitute a bond) and assign the value to each atom as there  $r_b$ . For Gaussian-  
 976 type orbitals (GTOs) and Slater-type orbitals (STOs), since they decay exponentially along radial  
 977 distance, we often set some precision threshold during data processing and find the largest bond in  
 978 off-diagonal blocks that is larger than the threshold value. The bond length will be considered as  
 979 our  $r_b$ .

980 The environmental cutoff  $r_e$  is very system dependent. This decides how large atomic/bond envi-  
 981 ronments relate to the mapping. This should follow the locality behaviour of the physical system.  
 982 For example, in typical periodic crystals such as semiconductors (Si, GaN, etc.), medals (Graphene),  
 983 and insulators (HfO<sub>2</sub>) the  $r_e$  are quite local, therefore, it is safe to set the  $r_e = r_b$ . However, when  
 984 systems experience strong nonlocality behaviour,  $r_e$  should be very large. One should carefully bal-  
 985 ance the efficiency of choosing a large  $r_e$  to ensure strict locality and the usage of a semi-local or  
 986 MPNN-based method.

987

988

## G LIMITATION

989

990

991 The SLEM model, benefiting from the Strictly localized design, performs better in accuracy and  
 992 transferability as demonstrated in various datasets. We acknowledge that such a localized hypothesis  
 993 is most suitable for describing periodic systems, which is commonly adopted in physics, chemistry  
 994 and material science research. For confined systems such as molecules, the absence of screening  
 995 effect could lead to long-term dependency that is uncovered within prefixed cutoff. In these cases,  
 996 the SLEM model wouldn't perform as well as in periodic cases. For generality, we also proposed  
 997 a semilocal model called LEM (Localized Equivariant Message-Passing), where the interaction be-  
 998 tween distant atoms is included but decays exponentially with their distance, with a trainable decay  
 999 factor. All the designed models are ready to use in our GitHub repository.

1000

## H FUTURE INVESTIGATION

1001

1002

1003 While SLEM demonstrates efficacy across various applications, several areas warrant further inves-  
 tigation:

1004

1005

1006

1007

1008

1009

1010

1011

1012

1013

1014

1015

1016

1017

1018

1019

- Sampling Methodology for Active Learning: Scientific computation tasks require high confidence in calculated results, which can be challenging for data-driven approaches. Developing a robust sampling workflow for active learning is essential for reliability. While techniques like uncertainty-driven sampling with Gaussian regression Vandermause et al. (2020) or model ensembles Zhang et al. (2020) have addressed confidence issues in machine learning force fields, designing a sampling workflow specifically for quantum operator models remains an open question.
- Software Integration for Post-Processing: Integrating the model with existing software is vital, especially for high-throughput calculations and large atomic systems beyond conventional DFT capabilities. An efficient, parallelizable solver for extracting physical quantities from the model's predictions is highly beneficial. While some software based on stochastic techniques Li et al. (2023); João et al. (2020) shows promise, an open-sourced and highly-optimized solution for non-orthogonal bases remains unavailable.

1020

1021

1022

1023

1024

1025